Application of the effective resistivity in MHD and Hall MHD simulations for collisionless magnetic reconnection

H. W. Zhang, Z. W. Ma*, and T. Chen

Institute for Fusion Theory and Simulation, Zhejiang University, Hangzhou 310027, China.

Abstract: The off-diagonal electron pressure terms are well-known for the frozen-in condition breakdown in collisionless magnetic reconnection, but are naturally kinetic and hard to employ in magnetohydrodynamics (MHD) simulations. Considering the inadequacy of MHD and Hall MHD in neglecting the important electron dynamics like inertia item and nongyrotropic pressure, we studied the kinetic features of electrons and ions in the diffusion region and suggested a new effective resistivity model involving basic dynamics of charged particles in diffusion region, which is found to be electron dominated in most of large ion-electron mass ratio cases [Z W Ma et al., Scientific Reports (2018) 8:10521]. The application of the effective resistivity in MHD and Hall MHD remarkably improves the simulation results compared with traditional models. Especially for the Hall MHD case with effective resistivity, the peak reconnection rate, major topological structures of the reconnection field and the current sheet are quite consistent with the reported particle-in-cell (PIC) and hybrid simulation results.

Keywords: Effective resistivity, Magnetic reconnection, Hall MHD

1

 $^{^{\}ast}$) Corresponding author: zwma@zju.edu.cn

1. Introduction

Magnetic reconnection accompanied with energy conversion and transport processes plays an important role in the topological evolution of plasmas in both space and laboratory. The magnetic reconnection concept was first suggested by Giovanelli [Giovanelli, 1946] in 1946 and the first well-known quantitative model was suggested by Sweet [Sweet, 1958] and Parker [Eugene N Parker, 1957]. However, for the predicted reconnection rate with the Y-type geometry of Sweet-Parker model is too slow to explain some explosive phenomena, such as, solar flares, magnetospheric substorms [Eugene Newman Parker, 1979], and tokamak disruptions [Taylor, 1986], it is replaced by the Petchek model that gives much faster reconnection rate by considering the X-type structure in a smaller diffusion region [Petschek, 1964]. Though the Petchek-type configuration has been confirmed in various situations, like locally enhanced resistivity simulation [Ugai, 1995] and Hall MHD simulation [Z Ma et al., 2015], the critical problem of Petchek model is that such a tiny structure can hardly form in most high-S collisionless plasmas simulations.

Resistivity is of vital importance in breaking down the frozen-in condition and resulting in the magnetic reconnection. However, in collisionless regime, the Spitzer resistivity [Spitzer, 2006] based upon electron-ion collision is too small to explain fast magnetic reconnection. A number of studies have been carried out to study the anomalous resistivity in collisionless magnetic reconnection. Ugai [Ugai, 1995] and Yokoyama et al. [Yokoyama and Shibata, 1994] independently develop fast reconnection mechanisms in simulations by setting resistivity as functions of relative electron-ion drift velocity. The current dependent anomalous resistivity model was studied by Otto [Otto, 2001] in MHD (magnetohydrodynamics) and Hall MHD simulations. Numata and Yoshida [Numata and Yoshida, 2002] suggested the concept of chaos-induced effective resistivity by analyzing the chaotic motion of particles around the magnetic null points. The off-diagonal elements of plasma pressure tensor are found to be responsible for the frozen-in condition breakdown in collisionless reconnection by Cai et al. [Cai and Lee, 1997] and Pritchett [Pritchett, 2001] in particlein-cell (PIC) simulations and by Kuznetsova et al. [Kuznetsova et al., 2001] in hybrid simulation. Apart from these simulation results, Ji et al. [Ji et al., 1999] refined the Sweet-Parker model by incorporating compressibility, downstream pressure, and an effective resistivity to explain the MRX experiment reconnection results.

Even though consensuses have been reached on the important role played by offdiagonal electron pressure terms in frozen-in condition breakdown, the inadequacy of MHD and Hall MHD in neglecting the important electron dynamics like inertia item and nongyrotropic pressure, leads to the difficulties of magnetohydrodynamics in describing small scale kinetic effects, especially the diffusion region. Based on these, we carried out theoretical studies on the formation mechanism for effective or anomalous resistivity in collisionless reconnection by investigating the kinetic features for the electron and ion. A new effective resistivity model involving charged particles dynamics in the diffusion region is suggested, and the mechanism is found to be electron dominated in most of large ion-electron mass ratio cases [Z W Ma et al., 2018]. The preliminarily successful applications of the effective resistivity model in both MHD and Hall MHD simulations indicate the importance of electron dynamics in the diffusion region. The time evolution of reconnection rate, topologies of the reconnection field and current sheet are significantly improved in both MHD and Hall MHD simulations after applying the effective resistivity. And we also found that the Hall MHD simulation results with effective resistivity applied are quite consistent with the PIC and hybrid simulation results.

The layout of the paper is given as follows. In Section 2, the brief derivation following Ref. [Z W Ma et al., 2018] for effective resistivity model is presented. And the Hall MHD model employed in simulations is given in Section 3. Section 4 gives the comparisons for the MHD simulations with or without effective resistivity. And similarly, section 5 gives the comparisons for the Hall MHD simulations with or without effective resistivity. Summary and discussion are presented in Section 6.

2. Effective resistivity

The out-of-plane flow velocity distributions of charged particles determine the topology of the central current sheet. Accordingly, the main idea is to analyze the characteristic motion for charged particles in reconnection magnetic field. As shown in **Figure 1**, in the diffusion region, the bulk velocity of plasma is mainly in out-of-plane

direction and the Lorentz force given by the reconnection field tends to change its motion direction towards downstream, which is equivalently to scattering the particles away the diffusion region and preventing the particle from being continuously accelerated by the electric field. As a result, the magnetic field induced scattering process gives out a characteristic time scale on the electric-particle acceleration. The statistical effect for all particles is equivalent to the enhancement of out-of-plane resistivity.

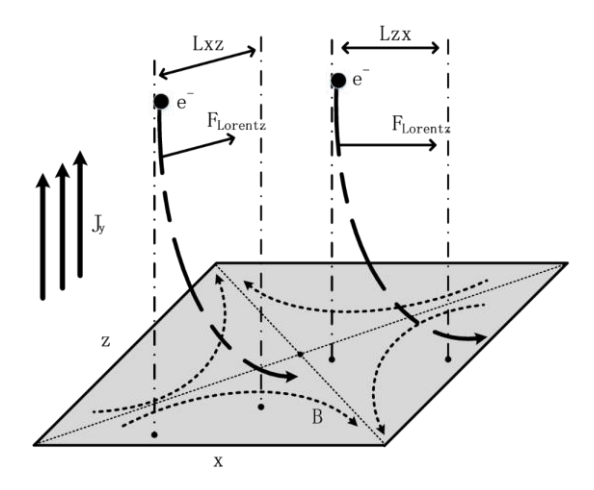


Figure 1. Electrons scattering by the magnetic field in the diffusion region.

To obtain the effective resistivity, we investigate the kinetic features for particles in electromagnetic field around the X-point. Without loss of generality, we first take the electron into consideration, the motion equation of electron due to electromagnetic force is

$$\frac{d\mathbf{v}_e}{dt} = -\frac{e}{m_e} \left(\frac{\mathbf{v}_e \times \mathbf{B}}{c} + \mathbf{E} \right). \tag{1}$$

Set the out-of-plane as y direction and the initial sheared magnetic field in x direction. Make the first order expansions for the magnetic field in x, z directions

$$\mathbf{B} = B_x \left(1 + \frac{z - z_0}{L_{xz}} + \frac{x - x_0}{L_{xx}} \right) \hat{\mathbf{x}} + B_z \left(1 + \frac{x - x_0}{L_{zx}} + \frac{z - z_0}{L_{zz}} \right) \hat{\mathbf{z}} + B_y \hat{\mathbf{y}},$$
(2)

$$L_{ij} = B_i / \partial_j B_i, (i, j = x, z), \tag{3}$$

where L_{xz} , L_{xx} , L_{zx} , respectively, are the characteristic lengths for B_x , B_z in x, z directions at a specified point (x_0, z_0) in the diffusion region.

To simplify the derivation and make Eq. (1) solvable, a few assumptions are given

as follow. First, the important component for electric field is E_y while the dominated magnetic field without guiding field is in-plane, accordingly, the in-plane electric field and out-of-plane magnetic field parts can be omitted in Eq. (1). Second, the evolutionary time scale for central current sheet (of the order of $10\,\tau_A$) is much longer than the electron scattering characteristic time scale (less than $1\,\tau_A$). Thus, we can estimate the average out-of-plane electron speed with $e\bar{v}_{ey}/m_e=J_{ey}/\rho_e$ to replace the v_{ey} component in Eq. (1), and ignore the time differential of v_{ey} . Thirdly, due to the directional characteristics of Lorentz force, L_{xz} , L_{zx} outweigh L_{xx} , L_{zz} much more. Finally, the sheared B_x leads to a quasi-oscillation in z direction while B_z results in the electron escaping in x direction, and these two processes are almost independent of one another in the diffusion region, thus the effective resistivity is mainly contributed by the reconnection field component B_z . Combing Eqs. (1), (2) and the above assumptions, the electron motion Eq. (1) can be reduced into the simple part in x direction as

$$\frac{d^2x}{dt^2} = \frac{J_{ey}B_z}{\rho_e L_{zx}c} (L_{zx} + x - x_0).$$
 (4)

An effective time scale for electric acceleration τ_e is defined as the duration that the electron spends on leaving the L_{zx} downstream away from the initial point by the magnetic field scattering process. It is simple to obtain the analytical solution x(t) and τ_e for $|x(\tau_e)-x_0|=L_{zx}$. Through further approximation analysis by ignoring v_{x0} around the X-point, τ_e is approximately equals to the form as

$$\tau_e \approx \sqrt{\frac{\rho_e L_{zx} c}{J_{ey} B_z}}. ag{5}$$

Afterwards, the out-of-plane variation tendencies of electron velocity v_{ey} and the current density J_{ey} around the X-point due to electric field E_y during τ_e are

$$\delta v_{ey} = \frac{e\tau_e E_y}{m_e},\tag{6}$$

$$\delta J_{ey} = \frac{n_e e^2 \tau_e E_y}{m_e}. (7)$$

And Eq. (7) indicates the effective resistivity around the X-point for J_{ey} in y direction

$$\eta_e = \frac{m_e^2}{e^2 \rho_e \tau_e} \tag{8}$$

The similar ion effective resistivity can be derived by considering the contribution of ion current density J_{iy} . Because the electric field E_y equals to the products of effective resistivity η_s (neglecting the Spitzer resistivity based on collisionless assumption) and current density J_{sy} for each species (character s indicating ion and electron), the electron and ion effective resistivity have the following relation

$$\frac{\eta_e}{\eta_i} = \frac{J_{iy}}{J_{ey}} \approx \sqrt{\frac{m_e J_{ey}}{m_i J_{iy}}}.$$
(9)

And the total effective resistivity η_{eff} equals to a correction of η_e . Thus, the final η_{eff} around the X-point is

$$\eta_{eff} \approx \frac{1}{1 + \sqrt{m_e J_{ey}/m_i J_{iy}}} \eta_e \approx \frac{1}{1 + \sqrt{m_e J_{ey}/m_i J_{iy}}} \cdot \frac{m_e^2}{e^2 \rho_e} \sqrt{\frac{J_{ey} B_z}{\rho_e L_{zx} c}}.$$
 (10)

In the approximation of $m_i / m_e \approx 1836$, we have

$$J_{v} \approx J_{ev} / 0.9245,$$
 (11)

$$\eta_{\text{eff}} \approx 0.9245 \eta_{\text{e}}.\tag{12}$$

Eqs. (11) and (12) demonstrate that in most cases with high ion-electron mass ratio, the electron dynamics plays a leading role in the total effective resistivity η_{eff} and the X-point current density J_y . According to Eq. (10), the effective resistivity η_{eff} strongly depends on the current density J_y , plasma density n_e and especially the spatial characteristic of reconnection magnetic field around the X-point B_z/L_{zx} . When fast magnetic reconnection occurs, B_z is enhanced and L_{zx} decreases, which may lead to an improvement on effective resistivity.

Similar but more detailed theoretical derivation and the corresponding quantitative verification for the effective resistivity by PIC simulation are reported in another published paper [Z W Ma et al., 2018].

3. Simulation model

The compressible 2.5D Hall MHD model is employed to study the fast collisionless magnetic reconnection with the application of effective resistivity. The 2.5 dimension

means all variables in y direction are uniform, i.e., $\partial/\partial y = 0$. The simulations are carried out in the Cartesian coordinate system within a rectangular box of $-L_x \le x \le L_x$, $-L_z \le z \le 0$. By introducing a magnetic flux function $\psi(x,z,t)$, the magnetic field is given by

$$\mathbf{B} = \hat{\mathbf{y}} \times \nabla \psi(x, z, t) + B_{v}(x, z, t)\hat{\mathbf{y}}.$$
 (13)

Then the compressible Hall MHD equations are [Z W Ma and Bhattacharjee, 2001]

$$\frac{\partial \rho}{\partial t} = -\nabla \cdot (\rho \mathbf{v}),\tag{14}$$

$$\frac{\partial (\rho \mathbf{v})}{\partial t} = -\nabla \cdot \left[\rho \mathbf{v} \mathbf{v} + \left(p + B^2 / 2 \right) \mathbf{I} - \mathbf{B} \mathbf{B} \right], \tag{15}$$

$$\frac{\partial \psi}{\partial t} = -\mathbf{v} \cdot \nabla \psi + \frac{1}{S_{tot}} J_{y} + \frac{d_{i}}{\rho} (\mathbf{J} \times \mathbf{B})_{y}, \qquad (16)$$

$$\frac{\partial B_{y}}{\partial t} = -\nabla \cdot \left(B_{y}\mathbf{v}\right) + \mathbf{B} \cdot \nabla v_{y} + \frac{1}{S_{spz}}\nabla^{2}B_{y} - d_{i}\nabla\left[\nabla \times \left(\frac{\mathbf{J} \times \mathbf{B} - \nabla p}{\rho}\right)\right]_{y},\tag{17}$$

$$\frac{\partial p}{\partial t} = -\nabla \cdot (p\mathbf{v}) - (\gamma - 1) p\nabla \cdot \mathbf{v} + \frac{1}{S_{tot}} J_y^2 + \frac{1}{S_{spz}} (J_x^2 + J_z^2), \tag{18}$$

where \mathbf{v} , \mathbf{B} , \mathbf{J} , ψ , ρ , p, \mathbf{I} are plasma velocity, magnetic field, current density, flux function, plasma mass density, thermal pressure and unit tensor, respectively. All variables are nondimensionalized as: $\mathbf{B}/B_0 \to \mathbf{B}$, $\mathbf{x}/d_i \to \mathbf{x}$, $\mathbf{v}/v_A \to \mathbf{v}$, $t/\tau_A \to t$, $\psi/(B_0d_i) \to \psi$, $\rho/\rho_0 \to \rho$, and $p(B_0^2/4\pi) \to p$, where B_0 is the initial asymptotic magnetic strength, d_i is the ion inertial length, $v_A = B_0/(4\pi\rho_0)^{1/2}$ is the Alfvén velocity, $\tau_A = d_i/v_A$ is the Alfvén time, ρ_0 is the asymptotic mass density, $\gamma = 5/3$ is the ratio of specific heats of plasma. The choice of d_i represents the intensity of Hall effect.

Note that due to the anisotropy of effective resistivity, two different Lundquist numbers S_{tot} and S_{spz} calculated from $S_{tot(spz)} = \tau_{R, tot(spz)} / \tau_A$ are applied respectively out-of-plane ($\tau_{R, tot} = 4\pi d_i^2 / c^2 \eta_{tot}$, and $\eta_{tot} = \eta_{spz} + \eta_{eff}$) and in-plane ($\tau_{R, spz} = 4\pi d_i^2 / c^2 \eta_{spz}$), where η_{spz} and η_{eff} are the Spitzer resistivity and effective resistivity, c is the light speed. For the Spitzer resistivity, a large constant Lundquist number ($S_{spz} \equiv 1000$) indicating low collision regime is applied in all simulation cases. And the effective resistivity induced S_{eff} is calculated in the following manner.

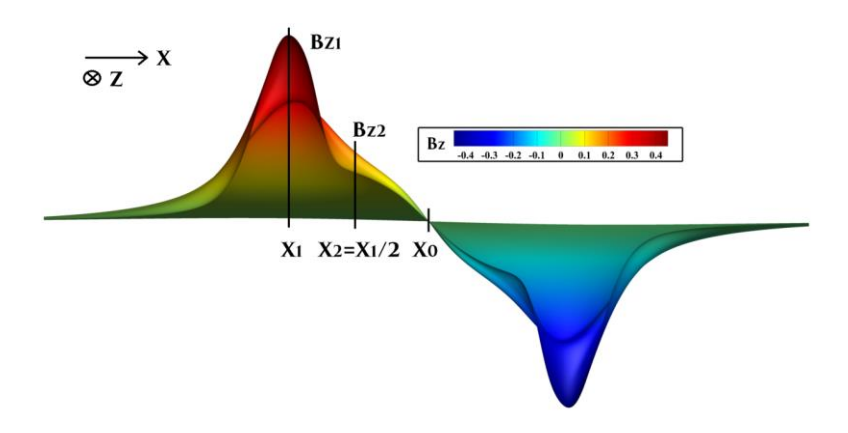


Figure 2. The heat map slice of a typical reconnection magnetic field B_z along the neutral line z = 0. The filed component maximum point is marked as (x_1, B_{z1}) , and the point of $(x_2 = x_1/2, B_{z2})$ is used to calculate the spatial variation of the reconnection magnetic field around the X point, that is, the value of B_z/L_{zx} in Eq. (10) is estimated with $|B_{z2}/(x_2-x_0)|$.

For a typical reconnection magnetic field B_z with the X-point at (x_0, z_0) , a heat map slice along the neutral line $(z = z_0)$ is shown in **Figure 2**. A specified point with the location $(x_2 = x_1/2, B_{z2})$ at the half length of the extreme B_z point (x_1, B_{z1}) is used to calculate the spatial variation of B_z around X-point, that is, the value of B_z/L_{zx} in Eq. (10) is estimated with $|B_{z2}/(x_2-x_0)|$. Of so choose the half length of extreme point as the characteristic reconnection field scale, is because B_z shows a fine linear trend spatially when $x_2 \le x \le x_0$, representing the gradient of B_z around the X-point simply and effectively. And by employing the electric neutrality assumption, the current density relation of Eq. (11) and the ion-electron mass ratio, we can replace J_{ey} and ρ_e at the X-point respectively with J_y and ρ in Eq. (10). After nondimensionalized with the above methods, the value of $S_{eff}(x,z,t)$ used in simulation is calculated by

$$\frac{1}{S_{eff}(x,z,t)} \approx \kappa \cdot \sqrt{\frac{J_y B_{z2}}{\rho^3 (x_2 - x_0)}} \cdot \exp\left[-\left(\frac{z - z_0}{\lambda_b}\right)^2 - \left(\frac{x - x_0}{x_2 - x_0}\right)^2\right]. \tag{19}$$

All parameters in Eq. (19) are dimensionless and can be replaced with their exact values in each simulation step directly. And under the assumption of ion-electron mass ratio and with Eqs. (10)-(12), the coefficient κ is a constant ($\kappa \approx 0.02$ for $m_i/m_e \approx 1836$). Besides, the characteristic spatial scales of the applied effective

Lundquist number are the real-time half width of the current sheet λ_b and the characteristic length $L_{zx} = |x_2 - x_0|$ of the reconnection magnetic field B_z .

The initial plasma velocity components v_x , v_y , v_z are set as zero. By solving equilibrium equations with the asymptotic plasma beta $\beta = 0.1$, the thermal pressure is given as

$$p = (1+\beta)B_0^2 / 2 - B^2 / 2. \tag{20}$$

A classical Harris current sheet with a half width of λ_b is chosen as the initial state

$$B_x = B_0 \tanh(z/\lambda_b), B_y = 0, B_z = 0.$$
 (21)

The initial mass density profile is given by

$$\rho(z) = \rho_0 + \rho_1 \operatorname{sech}^2(z/\lambda_\rho). \tag{22}$$

The mass density is set as $\rho_0 = 1.0$ and $\rho_1 = 0.2$. The characteristic scales for magnetic field and mass density are $\lambda_b = \lambda_\rho = 0.5$.

Eqs. (14)-(18) are solved with the fourth-order Runge-Kutta method in time and fourth-order finite difference method in space. The time step Δt is determined by Courant-Friedrichs-Lewy (CFL) condition. The simulation box is set as $L_x = 12.8$ and $L_z = 6.4$, with 640×500 grid points uniformly in x direction and nonuniformly in z direction $(dx = 0.04, dz_{min} = 0.01, dz_{max} = 0.02)$. Periodic boundary condition in x direction, free boundary condition at $z = -L_z$, and symmetric boundary condition at z = 0 are used. The reconnection rate γ_{rate} is calculated by the time derivation of the flux function or the product of resistivity and out-of-plane current density at the X-point, that is

$$\gamma_{rate} = \partial \psi / \partial t \approx \eta J_{v}. \tag{23}$$

The reconnection process is triggered with a small magnetic perturbation $(\delta \psi_0 = 0.01)$

$$\delta \psi = \delta \psi_0 \cos(\pi x / L_x) \cos(\pi z / 2L_z). \tag{24}$$

4. MHD simulation results

The effectivity resistivity given in Eq. (19) is firstly applied in the resistivity MHD model without Hall effect $(d_i = 0)$. For the case without effective resistivity, the coefficient κ in Eq. (19) set as 0 such that only the constant Spitzer resistivity

 $1/S_{spz} = 0.001$ is considered, and for the effective resistivity case, κ is set as 0.02 based on previous estimation.

The time evolution comparisons for the reconnection rate γ_{rate} , X-point current density J_y and the total resistivity η_{tot} are shown in **Figure 3**. The moments of peak reconnection t_{peak} are marked out with red lines respectively, $t_{peak} = 184\tau_A$ for η_{spz} case and $t_{peak} = 41\tau_A$ for η_{eff} case. After applying the effective resistivity, the reconnection rate is increased by over an order of magnitude compared with the η_{spz} case, and the time t_{peak} spent reaching the maximum reconnection rate is about one fourth of the η_{spz} case. The numerical diffusion is ignorable in η_{eff} case because the γ_{rate} calculated by $\partial \psi / \partial t$ (solid line) and ηJ_y (dashed line) in **Figure 3** (d) are almost the same, while too many iterations in η_{spz} case leads to the discrepancy in **Figure 3** (a). Because in η_{spz} case the resistivity shown in **Figure 3** (c) is a constant, the growth of reconnection rate requires great enhancement of the out-of-plane current density J_{y} at the X-point (with a peak value of 6.8, see **Figure 3** (b)). However, the situation in Figure 3 (e) is totally different for the η_{eff} case, the current density J_y shows a slow increase to the peak value of about 2.3 in the linear stage and after the start of fast reconnection $(t = 32\tau_A)$, J_v decreases quickly to a steady low level (\approx 1.55). Meanwhile, the total resistivity for the η_{eff} case, shown in **Figure 3** (f), lags a little behind the reconnection rate γ_{rate} but exhibits a similar rising tendency, and finally reaches a considerable value of 0.08, about a hundred times larger than the chosen Spitzer resistivity.

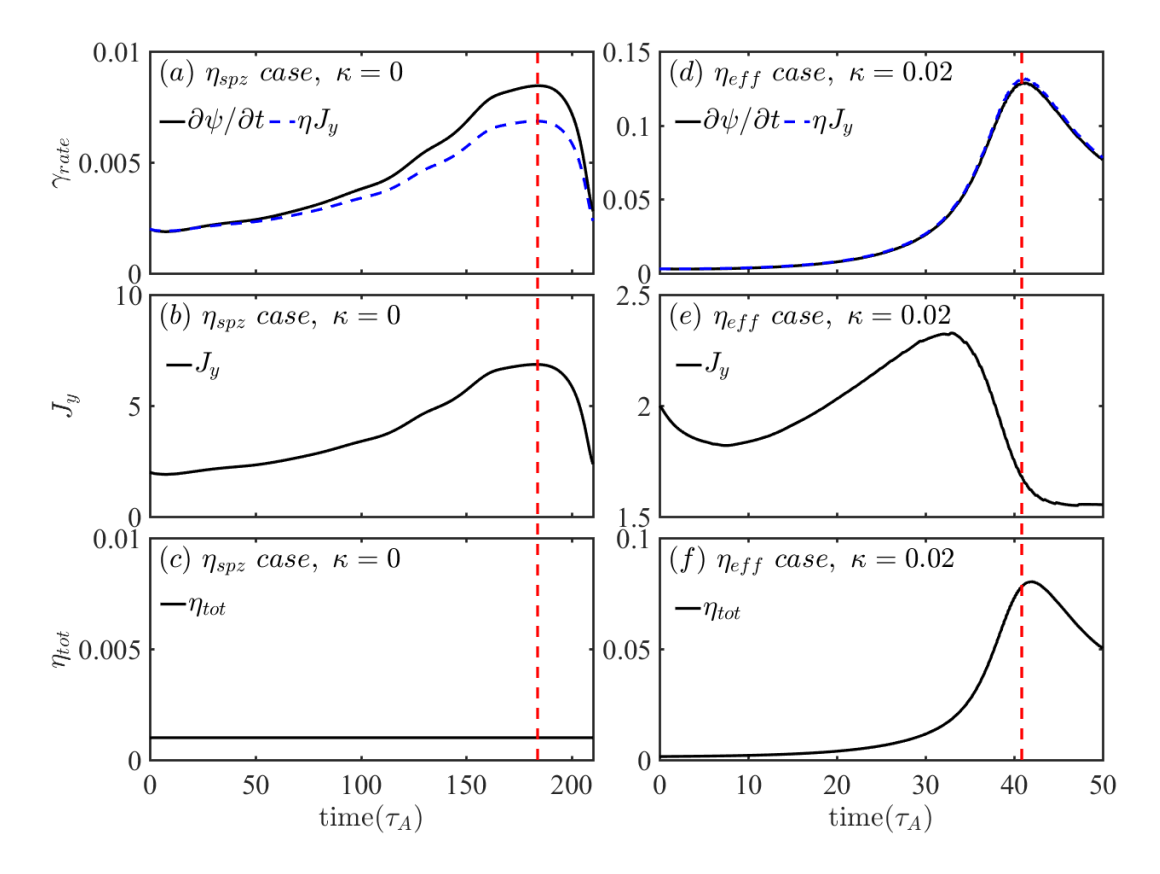


Figure 3. (MHD) time evolution results for (Left) Spitzer resistivity η_{spz} case with $\kappa = 0$: (a) reconnection rate calculated by $\partial \psi / \partial t$ (solid line) and ηJ_y (dashed line); (b) out-of-plane current density J_y at the X-point; (c) the total resistivity $\eta_{tot} \left(\eta_{eff} = 0 \right)$; (Right) Effective resistivity η_{eff} case with $\kappa = 0.02$: (d) reconnection rate calculated by $\partial \psi / \partial t$ (solid line) and ηJ_y (dashed line); (e) out-of-plane current density J_y at the X-point; (f) the total resistivity $\eta_{tot} \left(\eta_{eff} \neq 0 \right)$. Two red lines mark out the moments of peak reconnection respectively, $t_{peak} = 180\tau_A$ for η_{spz} case and $t_{peak} = 41\tau_A$ for η_{eff} case.

The distribution of out-of-plane current density J_y with magnetic field lines at the peak reconnection rate moments t_{peak} is plotted in **Figure 4** (a) for the η_{spz} case at $t_{peak} = 180\tau_A$, and **Figure 4** (b) for the η_{eff} case with $\kappa = 0.02$. The topological differences for the current sheets are significant. In the η_{spz} case, the current sheet is strongly compressed into a long and sharp line with the peak value of 6.8 at the X-point, and the geometry of the magnetic field in the reconnection region is a typical Y-type even though the separatrix angle downstream is considerable. As for the η_{eff} case, the current sheet is maintained at almost the same width as the initial situation, while the

current density J_y at the X-point falls off to a smaller value than the origin. The reason of a wider current sheet kept is due to the more effective resistive dissipation predicted by the Sweet-Parker model with the supplement of η_{eff} , that is $\lambda_b \approx L S_L^{-1/2}$. Besides, the magnetic field topology also changes greatly from the η_{spz} case, specifically, the geometry tends to transform from the Y-type into X-type, which leads to the strong increasement of the effective resistivity around the X-point and further greatly improves the reconnection rate. In more detail, the separatrix angle of the η_{eff} case is larger around the X-point but much smaller at downstream far from the diffusion region compared with the η_{spz} case, indicating the spontaneous localization of the reconnection field B_z and the corresponding strength of the effective resistivity η_{eff} in the diffusion region.

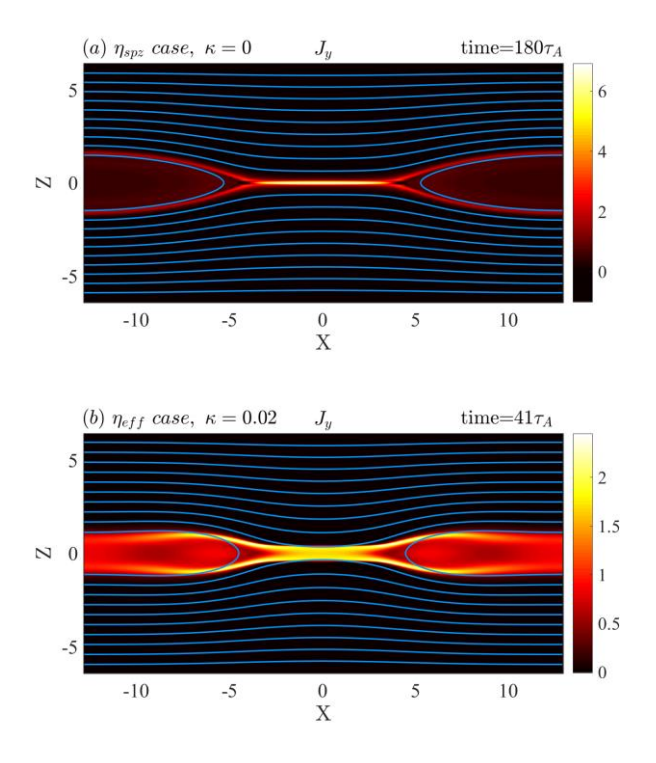


Figure 4. MHD results for the distribution of out-of-plane current density J_y with magnetic field lines at the moment of peak reconnection rate t_{peak} respectively for (a) Spitzer resistivity η_{spz} case, $\kappa = 0$, $t_{peak} = 180\tau_A$, (b) effective resistivity η_{eff} case, $\kappa = 0.02$, $t_{peak} = 41\tau_A$.

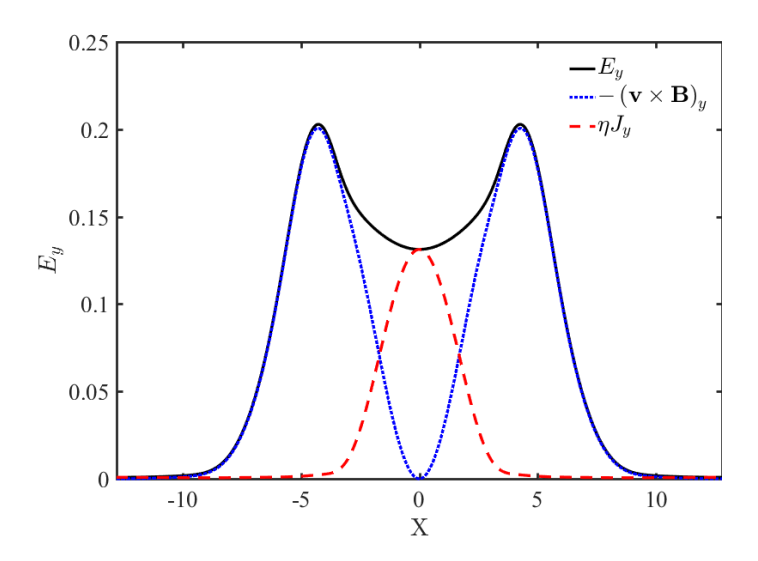


Figure 5. Contribution of terms in $E_y = -(\mathbf{v} \times \mathbf{B})_y + \eta J_y$ at the neutral line (z = 0) for the out-of-plane electric field at the peak reconnection time $t_{peak} = 41\tau_A$ of the effective resistivity η_{eff} MHD case, respectively, E_y with solid line, $-(\mathbf{v} \times \mathbf{B})_y$ with dotted line, and ηJ_y with dashed line.

Figure 5 shows the contribution of terms for the out-of-plane electric field as $E_y = -(\mathbf{v} \times \mathbf{B})_y + \eta J_y$ (the Hall term is neglected as $d_i = 0$) at the neutral line (z = 0), for the η_{eff} case at the peak reconnection rate $t_{peak} = 41\tau_A$. Clearly, the out-of-plane electric field E_y is mainly contributed by ηJ_y around the X-point where the magnetic field strength is ignorable, while outside the diffusion region, $-(\mathbf{v} \times \mathbf{B})_y$ plays the leading role.

Through the above comparisons, the traditional resistivity MHD model merely considering the negligible Spitzer resistivity η_{spz} is bound to result in the abnormal growth of current density J_y at the X-point and strong compression on the sheet width λ_b , leading to a unwished reinforce on the shear reconnecting field $(B_x \propto J_y \lambda_b)$. However, after applying the effective resistivity η_{eff} , the reconnection rate depends on more factors included in the expression of η_{eff} given by Eq. (10) other than the X-point J_y , especially the spatial features of the reconnection field B_z in the diffusion region. Moreover, since the considerable effective resistivity η_{eff} generally increases the resistive dissipation rate and the enhanced reconnection field B_z is also equivalent to generating an inverse J_y in the diffusion region, the decrease of J_y at the X-point is logical and understandable.

5. Hall MHD simulation results

We now report the simulation results of the Hall MHD cases with or without effective resistivity η_{eff} , all parameters for the η_{spz} case ($\kappa=0$) and η_{eff} case ($\kappa=0.02$) with Hall effect in this section are the same as the previous settings except for the ion inertial length is replaced by $d_i=1.0$.

We give out the time evolution comparison results of the reconnection rate γ_{rate} , X-point current density J_y and the total resistivity η_{tot} for η_{spz} case and η_{eff} case in **Figure 6**. And the moments for the peak reconnection rate t_{peak} are marked out with red lines. As shown in **Figure 6** (a) and (d), the employ of effective resistivity η_{eff} in Hall MHD model doesn't change a lot in the peak reconnection rate calculated by $\partial \psi / \partial t$, both about 0.25, but the rates calculated by ηJ_{ν} (dashed lines in **Figure 6** (a) and (d)) show a significant difference. For the η_{spz} case, the peak value of $\partial \psi / \partial t$ (≈ 0.25) is far greater than ηJ_{ν} (≈ 0.01), which indicating terrible numerical diffusion at the X-point. However, the situation in η_{eff} case is much better. The peak reconnection rates in **Figure 6** (d) represented by $\partial \psi / \partial t$ (≈ 0.25) and ηJ_{ν} (≈ 0.2) are quite close to each other. Therefore, the numerical diffusion in Hall MHD simulation is acceptable after applying the effective resistivity η_{eff} . In addition, the effective resistivity η_{eff} also helps shorten the time taken to reach the peak reconnection rate by about $12 \tau_A$. It is also found that the change of coefficient κ (κ from 0.1 to 0.5, corresponding m_i / m_e from 300 to 5000) only shortens the peak reconnection rate time but makes little difference on the peak reconnection rate in Hall MHD simulation with effective resistivity (not plotted), which is consistent with the conclusion that the peak reconnection rate weakly depends on the ion-electron mass ratio [Pritchett, 2001; Shay et al., 2007]. The differences on the time evolutions of the X-point current density J_{y} (Figure 6 (b) and (e)) and the total resistivity η_{tot} (Figure 6 (c) and (f)) for two resistivity cases are similar to the discussions in previous section for the MHD results shown in Figure 3 and therefore, we won't go into more details here.

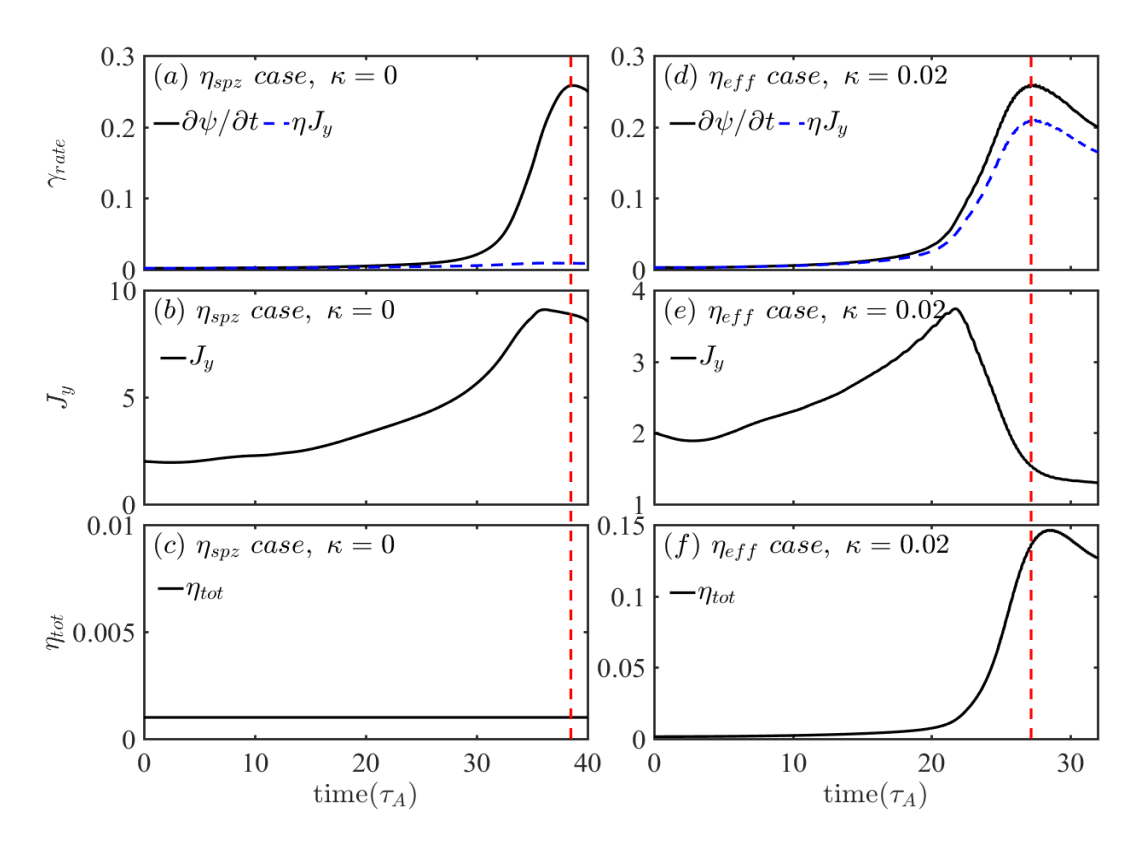


Figure 6. (Hall MHD) time evolution results for (Left) Spitzer resistivity η_{spz} case with $\kappa = 0$: (a) reconnection rate calculated by $\partial \psi / \partial t$ (solid line) and ηJ_y (dashed line); (b) out-of-plane current density J_y at the X-point; (c) the total resistivity $\eta_{tot} \left(\eta_{eff} = 0 \right)$; (Right) Effective resistivity η_{eff} case with $\kappa = 0.02$: (d) reconnection rate calculated by $\partial \psi / \partial t$ (solid line) and ηJ_y (dashed line); (e) out-of-plane current density J_y at the X-point; (f) the total resistivity $\eta_{tot} \left(\eta_{eff} \neq 0 \right)$. Two red lines mark out the moments of peak reconnection respectively, $t_{peak} = 39\tau_A$ for η_{spz} case and $t_{peak} = 27\tau_A$ for η_{eff} case.

Figure 7 shows the distribution of current sheet J_y with magnetic field lines for two cases at the peak reconnection rate time. Obvious X-type magnetic field geometries can be seen for both cases in **Figure 7** (a) and (b), which are consistent with the high reconnection rate of about 0.25. Nonetheless, due to the different dissipative effects of the two resistivity models, the topologies of the corresponding current sheets are notably different from each other, a wider current sheet is maintained in the η_{eff} case shown in **Figure 7** (b) for the reason of larger resistive dissipation, while a sharp current peak forms in the η_{spz} case in **Figure 7** (a). And the situations for the current sheet in the vicinity of the X-point are similar to the MHD comparisons discussed in the

previous section. Besides, the splitting phenomenon of current sheet downstream at $x \approx \pm 5$ can be seen in the η_{eff} case, which is quite similar to results reported by the particle-in-cell simulations [Fujimoto and Sydora, 2008; Hesse et al., 2001a; Hesse and Winske, 1998] (a comparison of J_y distributions at the peak reconnection rate moments for η_{eff} Hall MHD results with $\kappa = 0.04$ and the corresponding PIC result with $m_i/m_e = 400$ is given in Figure 9) and hybrid simulations [Kuznetsova et al., 2001].

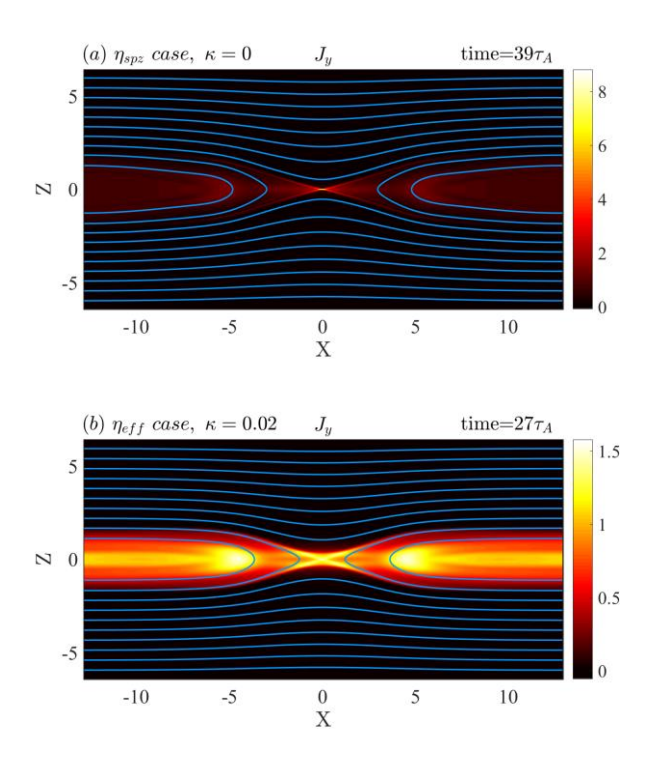


Figure 7. Hall MHD results for the distribution of out-of-plane current density J_y with magnetic field lines at the moment of peak reconnection rate t_{peak} respectively for (a) Spitzer resistivity η_{spz} case, $\kappa = 0$, $t_{peak} = 39\tau_A$, (b) effective resistivity η_{eff} case, $\kappa = 0.02$, $t_{peak} = 27\tau_A$.

Next, we investigated the different roles played by the electron and ion. We estimate the electron and ion flow velocities respectively by $\mathbf{v_e} \approx \mathbf{v} - \mathbf{J}/n$ and $\mathbf{v_i} \approx \mathbf{v}$ (assuming $n = n_i = n_e$). Then the out-of-plane current density for ions and electrons are estimated at the X-point, where $J_{ey} \approx 0.952 J_y$ and $J_{iy} \approx 0.048 J_y$, therefore, the electron current density dominant assumption at the X-point in Eq. (11) is self-consistent with the η_{eff} Hall MHD simulation result and also confirmed by the PIC

simulations with large ion-electron mass ratio [Hesse et al., 2001a; Pritchett, 2001]. The in-plane electron and ion flow vectors are plotted in Figure 8 respectively in the upper and lower half plane. In the upstream outside the diffusion region, both electrons and ions are magnetized and driven inward as the $\mathbf{E} \times \mathbf{B}$ drift. However, as close to the diffusion region $(|z| \approx d_i)$, the ion firstly beaks away from the magnetic field lines and is accelerated towards the downstream, while the electron is still frozen to the magnetic field lines. And the electron moves much closer to the X-point before leaving the diffusion region, that's also why the out-of-plane current density at the X-point is dominated by electrons. And the electron mainly flows in and out the diffusion region along the separatrix, corresponding to the formation of the quadrupole B_v field seen in Hall MHD or PIC simulations as shown in Figure 10. And inside the diffusion region, where $\mathbf{E} + \mathbf{v_e} \times \mathbf{B}/c = 0$ breaks down, due to the inhomogeneity of reconnection field B_z , the electrons are scattered or speeded away quickly from the X-point with the characteristic time scale of τ_e expressed in Eq. (5), thus, the continuous out-of-plane electric accelerating for electron is not permitted in the diffusion region, which is equivalent to the role played by the effective resistivity η_{eff} .

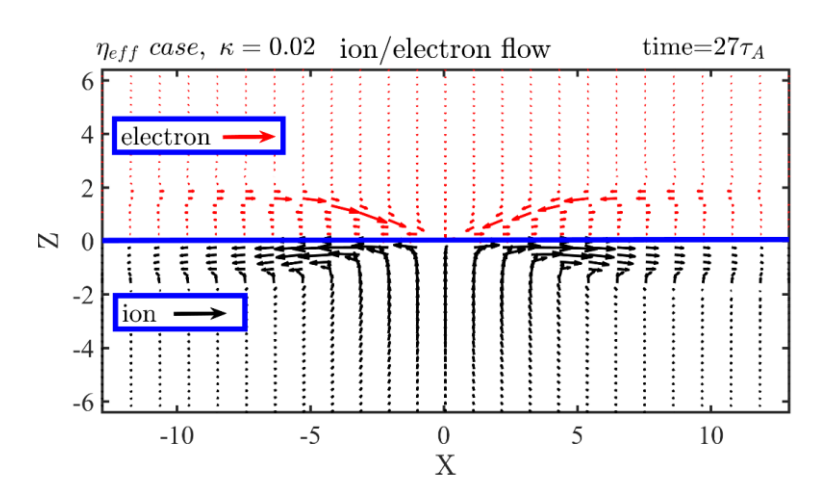


Figure 8. The in-plane velocities of the η_{eff} case at the $t_{peak} = 27\tau_A$, respectively for electron flow with red vectors (plotted in the upper half plane) and ion flow with black vectors (plotted in the lower half plane).

Figure 11 shows the contribution of terms for the out-of-plane electric field as $E_y = -(\mathbf{v_e} \times \mathbf{B})_y + \eta J_y$ at the neutral line (z=0), for the η_{eff} case at the peak reconnection rate $t_{peak} = 27\tau_A$. Clearly, the out-of-plane electric field E_y is mainly

contributed by ηJ_y around the X-point where the magnetic field strength is ignorable, while outside the diffusion region, $-(\mathbf{v_e} \times \mathbf{B})_y$ plays the leading role. The discontinuity of E_y in the vicinity of X-point is marked out with an ellipse, where an unwanted gap of $\Delta E_y \approx 0.05$ compared with the asymptotic value is seen, which is close to the difference between two methods calculated reconnection rate $\partial \psi / \partial t$ and ηJ_y shown in **Figure 6** (d). It might be because the relatively large but necessary numerical diffusion for the code's stability used in the Hall MHD simulation impedes the growth of ηJ_y at the X-point, that is, an equivalent numerical resistivity η_{num} should be considered in the diffusion region so that $(\eta_{eff} + \eta_{spz} + \eta_{num})J_y = \partial \psi / \partial t$ will be satisfied. Thus, we can expect that in an ideal case without numerical diffusion and with precisely calculated effective resistivity in diffusion region, the distribution of calculated E_y in **Figure 11** will be much smoother as the MHD situation in **Figure 5**.

For more direct comparisons with PIC simulations, the out-of-plane current density J_y with magnetic field lines at peak reconnection rate time is shown in **Figure 9** (a) for $\kappa = 0.04$ in effective resistivity Hall MHD case and **Figure 9** (b) is the PIC result with $m_t/m_e = 400$, correspondingly. Though the application of effective resistivity greatly improves the Hall MHD simulation results, we still have to admit some topological differences between the PIC and effective resistivity applied Hall MHD results, such like, the thinner diffusion region and more concentrated but larger J_y value downstream in PIC result, while compared with situations of J_y , the quadrupole B_y field in η_{eff} Hall MHD result is much consistent with the PIC result both for the magnitude and distribution, see **Figure 10**. Consequently, the effective resistivity mainly corrects the important electron mechanism in the diffusion region on a macro level, i.e., the X-point current density dissipation and the anomalous resistivity generation, but at the outside, like downstream regions, discrepancies still exist in Hall MHD and PIC simulations due to their different physical description methods.

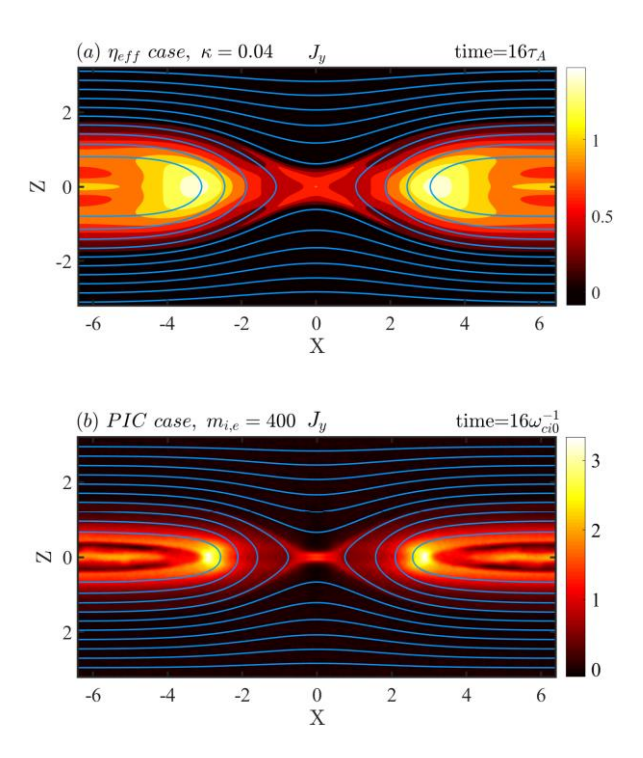


Figure 9. The distribution of out-of-plane current density J_y with magnetic field lines at the peak reconnection time respectively for (a) the η_{eff} Hall MHD result with $\kappa = 0.04$ and (b) PIC simulation with $m_i/m_e = 400$.

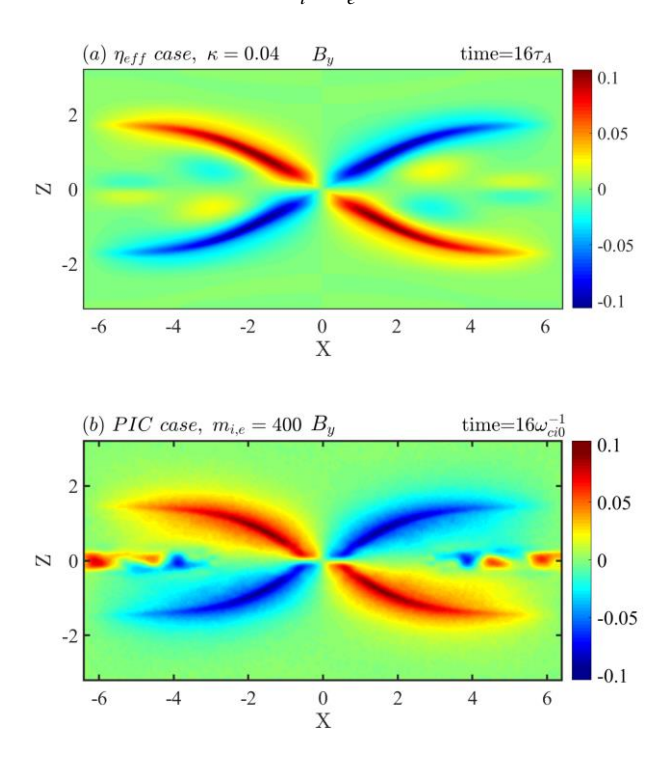


Figure 10. The distribution of quadrupole B_y filed at the peak reconnection time respectively for (a) the η_{eff} Hall MHD result with $\kappa = 0.04$ and (b) PIC simulation with $m_i/m_e = 400$.

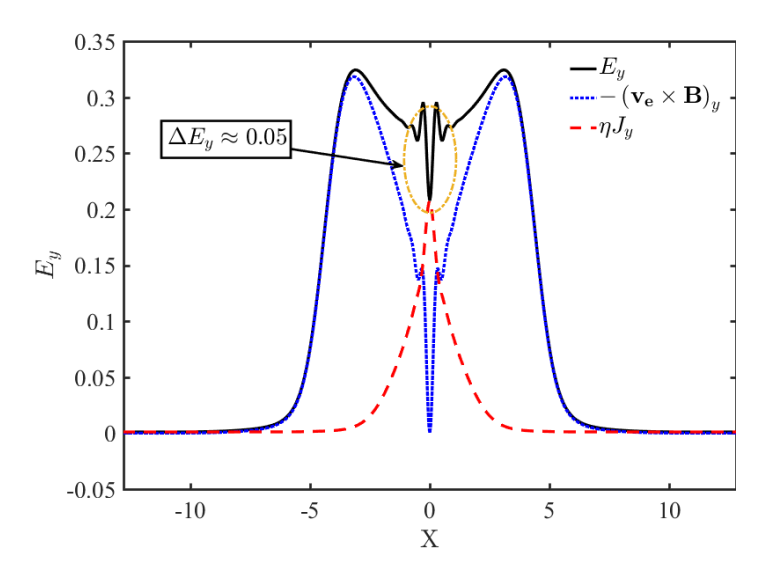


Figure 11. Contribution of terms in $E_y = -(\mathbf{v_e} \times \mathbf{B})_y + \eta J_y$ at the neutral line (z = 0) for the out-of-plane electric field at the peak reconnection time $t_{peak} = 27\tau_A$ of the effective resistivity η_{eff} Hall MHD case, respectively, E_y with solid line, $-(\mathbf{v_e} \times \mathbf{B})_y$ with dotted line, and ηJ_y with dashed line.

Conclusively, the Hall term improves the reconnection rate by including the charge separation effect in the presence of Hall current outside the diffusion region, where the electron fluid is still frozen in the magnetic field lines but the ions become demagnetized. And the equally important electron mechanism inside the diffusion region is repeatedly verified in the form of the off-diagonal electron pressure terms in generalized Ohm' law by PIC simulations [Cai and Lee, 1997; Hesse et al., 2001b; Pritchett, 2001] and lab experiments [Fox et al., 2017]. Therefore, at some level, the comparisons for Hall MHD simulation results above indicates the preliminary success of replacing electron kinetic effects in the diffusion region by effective resistivity. Therefore, due to the out of sync in demagnetizing for different charges, the ion and electron plays separately major role in the Hall region and diffusion region, and together to enhance the collisionless reconnection process.

6. Discussions and conclusions

The magnetohydrodynamics that has omitted the electron inertial term and the anisotropy of electron pressure, loses quite important electron contributions to the reconnection process inside the diffusion region. To complete the traditional MHD and

Hall MHD model in magnetic reconnection simulations, we considered the kinetic features of electron in a typical reconnection field and sequentially suggested an effective resistivity model [Z W Ma et al., 2018], which is simple and applicable in magnetohydrodynamics simulations. The MHD results demonstrate the effectiveness of this new resistivity model in speeding up the reconnection process and improving the peak reconnection rate without Hall effect. The topologies of the reconnection field (tends to X-type) and current sheet (wider and lower) are more reasonable and logical compared with the traditional MHD situation. After employing the Hall term in simulation, the peak reconnection rate is further enhanced up to the value of 0.2~0.25, which is close to the PIC results. And the X-type magnetic geometry, obvious current sheet splitting and ion-electron separation phenomena that are similar to the PIC results can be clearly seen in Hall MHD simulation with the application of effective resistivity.

We hope the basic theory and application of the effective resistivity model could provide new insights to explain the anomalous resistivity problem in breaking down the frozen-in condition during the collisionless reconnection process, and also in a very sort of pragmatic sense, the effective resistivity model could help complete the MHD and Hall MHD reconnection models which used to be inadequate to describe vital small-scale physics for the loss of electron contributions especially in the reconnection diffusion region.

References

Cai, H.-J., and L. Lee (1997), The generalized Ohm's law in collisionless magnetic reconnection, *Physics of Plasmas (1994-present)*, 4(3), 509-520.

Fox, W., F. Sciortino, A. v. Stechow, J. Jara-Almonte, J. Yoo, H. Ji, and M. Yamada (2017), Experimental Verification of the Role of Electron Pressure in Fast Magnetic Reconnection with a Guide Field, *Phys. Rev. Lett.*, *118*(12), 125002.

Fujimoto, K., and R. D. Sydora (2008), Electromagnetic particle-in-cell simulations on magnetic reconnection with adaptive mesh refinement, *Comput. Phys. Commun.*, 178(12), 915-923.

Giovanelli, R. (1946), A theory of chromospheric flares, *Natur*, 158(4003), 81-82.

Hesse, M., J. Birn, and M. Kuznetsova (2001a), Collisionless magnetic reconnection: Electron processes and transport modeling, *Journal of Geophysical Research: Space Physics*, 106(A3), 3721-3735.

Hesse, M., M. Kuznetsova, and J. Birn (2001b), Particle-in-cell simulations of three-dimensional collisionless magnetic reconnection, *Journal of Geophysical Research: Space Physics (1978–2012)*, *106*(A12), 29831-29841, doi:10.1029/2001JA000075.

- Hesse, M., and D. Winske (1998), Electron dissipation in collisionless magnetic reconnection, *Journal of Geophysical Research: Space Physics*, 103(A11), 26479-26486.
- Ji, H., M. Yamada, S. Hsu, R. Kulsrud, T. Carter, and S. Zaharia (1999), Magnetic reconnection with Sweet-Parker characteristics in two-dimensional laboratory plasmas, *Physics of Plasmas (1994-present)*, 6(5), 1743-1750.
- Kuznetsova, M. M., M. Hesse, and D. Winske (2001), Collisionless reconnection supported by nongyrotropic pressure effects in hybrid and particle simulations, *Journal of Geophysical Research: Space Physics*, 106(A3), 3799-3810.
- Ma, Z., L. Wang, and L. Li (2015), Reconnection dynamics with secondary tearing instability in compressible Hall plasmas, *Physics of Plasmas (1994-present)*, 22(6), 062104.
- Ma, Z. W., and A. Bhattacharjee (2001), Hall magnetohydrodynamic reconnection: The Geospace Environment Modeling challenge, *J Geophys Res-Space*, 106(A3), 3773-3782, doi:10.1029/1999ja001004.
- Ma, Z. W., T. Chen, H. W. Zhang, and M. Y. Yu (2018), Effective Resistivity in Collisionless Magnetic Reconnection, *Scientific Reports*, 8(1), 10521, doi:10.1038/s41598-018-28851-7.
- Numata, R., and Z. Yoshida (2002), Chaos-induced resistivity in collisionless magnetic reconnection, *Phys. Rev. Lett.*, 88(4), 045003.
- Otto, A. (2001), Geospace Environment Modeling (GEM) magnetic reconnection challenge: MHD and Hall MHD—constant and current dependent resistivity models, *Journal of Geophysical Research: Space Physics*, 106(A3), 3751-3757.
- Parker, E. N. (1957), Sweet's mechanism for merging magnetic fields in conducting fluids, *J. Geophys. Res.*, 62(4), 509-520.
- Parker, E. N. (1979), Cosmical magnetic fields: Their origin and their activity, Oxford, Clarendon Press; New York, Oxford University Press, 1979, 858 p.
- Petschek, H. E. (1964), Magnetic field annihilation, NASAS, 50, 425.
- Pritchett, P. L. (2001), Geospace Environment Modeling magnetic reconnection challenge: Simulations with a full particle electromagnetic code, *J Geophys Res-Space*, 106(A3), 3783-3798, doi:10.1029/1999ja001006.
- Shay, M., J. Drake, and M. Swisdak (2007), Two-scale structure of the electron dissipation region during collisionless magnetic reconnection, *Phys. Rev. Lett.*, 99(15), 155002.
- Spitzer, L. (2006), Physics of fully ionized gases, Courier Corporation.
- Sweet, P. (1958), In B. Lehnert, editor, *Electromagnetic Phenomena in Cosmical Physics*, 123.
- Taylor, J. (1986), Relaxation and magnetic reconnection in plasmas, *Rev. Mod. Phys.*, 58(3), 741.
- Ugai, M. (1995), Computer studies on plasmoid dynamics associated with the spontaneous fast reconnection mechanism, *Phys. Plasmas*, 2(9), 3320-3328.
- Yokoyama, T., and K. Shibata (1994), What is the condition for fast magnetic reconnection?, *The Astrophysical Journal*, 436, L197-L200.